Stability analysis of two-dimensional models of three-dimensional convection

H. S. Greenside
Plasma Physics Laboratory, Princeton University, P.O. Box 451, Princeton, New Jersey 08544

M. C. Cross
Department of Physics, California Institute of Technology, Pasadena, California
(Received 28 November 1983; revised manuscript received 29 October 1984)

Analytical and numerical methods are used to study the linear stability of spatially periodic solutions for various two-dimensional equations which model thermal convection in fluids. This analysis suggests new model equations that will be useful for investigating questions such as wave-number selection, pattern formation, and the onset of turbulence in large-aspect-ratio Rayleigh-Bénard systems. In particular, we construct a nonrelaxational model that has stability boundaries similar to those calculated for intermediate Prandtl-number fluids.

I. INTRODUCTION

The onset of time-dependent flows in large-aspect-ratio Rayleigh-Bénard convection cells show several features which suggest that a more complete understanding of the fluid dynamics may be reached than in smaller cells.[1] In particular, in large-aspect-ratio cells (i.e., those of lateral dimension large compared to the wavelength of the spatially periodic convecting solution) and at low values of the Prandtl number $\lesssim 10$ (the ratio of the viscosity of the fluid to the thermal conductivity), chaotic time dependence is observed either at driving strengths close to the initial occurrence of the convecting state, or at only slightly stronger driving at the first instability of a stationary convecting state.[2,3] At these low driving strengths, the fluid flows do not show structures on the short length scales which are typically found at the onset of chaotic time dependence at stronger driving in small cells. Indeed the onset of chaotic dynamics has been tentatively associated with the occurrence of the skewed-varicose instability, an interesting long-wavelength instability with a spatial dependence neither entirely longitudinal nor transverse to the local wave vector.[2] The subsequent motion is a slow wandering of the spatial structure on time scales much larger than the time scale of the convective flow itself (the vertical thermal diffusion time). Such motion may well be easier to understand than the coupled, highly nonlinear oscillators characteristic of the time dependence in small cells. In addition, since the chaotic motion in large cells is probably not described by low dimensional attractors, its study may provide further insights into the development of turbulent motion involving many independent degrees of freedom.

The two most obvious approaches for understanding the slow chaotic dynamics in large cells, analytic expansions, and numerical simulations are not yet practical to pursue. An analytic formalism exists for calculating the slow dynamics of distortions on length-scales large compared to the basic periodicity (roll size) from the underlying Boussinesq equations.[4] The dynamical equation so obtained leads to the prediction that defects in the roll patterns, such as dislocations, will develop. This is indeed seen experimentally. Since defects involve structure on the roll length scale, their dynamics cannot be treated within this formalism. On the other hand, a numerical simulation of the five three-dimensional Boussinesq equations, for *long* times and in *large* cells with realistic boundary conditions, remains well beyond the scope of present computing power.

In view of these difficulties we, and others, have proposed analyzing two-dimensional model equations that may be numerically integrated and systematically studied with greater ease. The aim is to study model equations that adequately reproduce the long-length-scale dynamics of convective roll states as would be predicted from the Boussinesq equations and which also allow the calculation of dynamics on the roll length scale. A complete convecting pattern, including defects, may then be simulated. It is hoped that the *details* of the roll-length-scale dynamics, probably poorly approximated in these models, is not crucial in describing the slow dynamics in a large cell near the onset of convection.

In this paper, we investigate the stability properties of a large class of model equations and present a two-dimensional model that reproduces the long-length-scale dynamics of the Boussinesq equations in that it has a similar linear-stability diagram. Since the particular features of the fluid equations that give rise to observed chaotic behavior are not yet understood, there is no *a priori* way of deriving suitable model equations. We propose that a systematic study for the models of the instabilities that limit the band of stable wave numbers at each value of the control parameter, and a comparison with the stability diagram of the fluid equations, may provide a useful way to select a model for detailed analysis. Our proposal is motivated by the considerable insight provided by Busse and co-workers[1,5] who numerically studied the linear stability of the fully nonlinear, stationary, singly periodic solutions of the Boussinesq equations for different Rayleigh numbers R and wave numbers K. Although these calculations do not strictly apply to convection in finite experimental geometries (the periodic solu-

tions correspond to an infinite aspect ratio), they have proved to be a useful guide for qualitatively understanding instabilities observed experimentally.

The models we present satisfy three important criteria. First, they match at lowest order the singular perturbation expansion of the Boussinesq equations at the convective threshold.[6,7] Close enough to onset, they therefore have the same dynamics and instabilities in slow variables as the Boussinesq equations. Second, the models are rotationally invariant. Unlike the amplitude equations to which they reduce near threshold, the coordinate system does not have to be oriented locally with respect to the roll axis. This is important for global studies of defects and textures in the presence of lateral walls. Third, the models are not restricted to be relaxational; their solutions can have an oscillatory or nonperiodic time dependence. This is a necessary requirement for the onset of turbulence in large-aspect-ratio cells. In addition we follow Siggia and Zippelus[8] in modeling the singular mean drift effects encountered in finite Prandtl-number fluids by an additional field representing the vertical vorticity. With this modification the models do indeed show the important skewed-varicose instability.

A particular goal in our study of various models is to find a model for which the skewed-varicose instability has the same qualitative stability boundary as that calculated by Busse and Clever for finite-Prandtl-number convection,[5] namely, the boundary $R(K)$ is a decreasing function for increasing wave number K. While this can be achieved, as we show below, special care must be taken to ensure that short-wavelength instabilities do not preempt the skewed varicose by occurring at lower Rayleigh numbers. This occurs, for example, in the model proposed by Manneville[9] if the short-wavelength filtering procedure we suggest below is not included.

II. DISCUSSION OF MODELS

The study of model equations in convection was initiated by Swift and Hohenberg who used the equation

$$\partial_t\psi=[r-(\nabla^2+1)^2]\psi-\psi^3 \tag{2.1}$$

to investigate the nature of the transition to the convecting state.[10] Here ∂_t denotes a time derivative, ∇ is the two-dimensional (horizontal) gradient and $\psi(x,y,t)$ is a real field of the horizontal coordinates (x,y) and time t. The parameter r is the control or bifurcation parameter. Equation (2.1) shows a transition at $r=0$ from a state with $\psi=0$ (associated with the conducting state with zero fluid velocities) to a spatially periodic state for $r>0$ with critical wave number $K_c=1$ (the convecting state). The equation may be derived for $r\to 0$ as a rotationally invariant equation that reproduces to lowest nontrivial order the perturbation expansion of the Navier-Stokes equations near threshold.[11] In this limit the temperature field, for example, is given by $T(x,y,t)\simeq\psi(x,y,t)T_0(z)$ with T_0 a known function.

The analysis of Eq. (2.1) as a model equation for $r\lesssim 1$ has yielded considerable insight into questions of pattern formation and wave-number selection.[12] However the simple structure of Eq. (2.1) leads to certain undesirable features in this regime. Firstly, the dynamics derives from a potential, i.e., there exists a functional $V[\psi]$, bounded below, such that

$$\partial_t\psi=\frac{-\delta V}{\delta\psi}\ , \tag{2.2}$$

with

$$V=\int\int dx\,dy\{-\tfrac{1}{2}r\psi^2+\tfrac{1}{4}\psi^4+\tfrac{1}{2}[(\nabla^2+1)\psi]^2\}\ . \tag{2.3}$$

This implies the motion is relaxational and that no persistent dynamics occurs.[13] Secondly, the simple nonlinear term ψ^3, chosen solely to reproduce the behavior to lowest order near threshold, leads to stability boundaries $K_\pm$ that are monotonic functions of r, in contrast to the behavior for the fluid equations.[12] Furthermore, the structure of the gradient terms does not allow the skewed-varicose instability, which depends on the singular nature of a slow gradient expansion about a spatially periodic solution.

The first class of equations we discuss are generalizations of the Swift-Hohenberg equation:

$$\partial_t\psi=[r-(\nabla^2+1)^2]\psi-a\psi^3-b\psi(\nabla\psi)^2+c\psi^2\nabla^2\psi\ . \tag{2.4}$$

The extra nonlinear terms allow more flexibility in the choice of the behavior of the stability boundaries by varying the coefficients a, b, and c. It is known, for example, that the cubic nonlinear term $a\psi^3$ in the Swift-Hohenberg equation does not directly correspond to the fluid equations even near threshold. The threshold expansion of the Boussinesq equations shows that the correct nonlinear term is, in fact, a cubic sum of Fourier modes for which there is no local real-space expression.[11] Thus the cross-roll instability of the Swift-Hohenberg equation will not coincide with that calculated from the fluid equations even close to threshold. The additional terms included in Eq. (2.4) may be suggested as the terms in a gradient expansion of the kernel and may be used to include more of the correct structure. (For $b=-c$ the equation remains potential.) On the other hand, Manneville has suggested[9] that the choice $a=b=1$, $c=0$ gives a better description of convection between free slip boundaries, although his derivation is not systematic in any small parameter. Alternatively, for $b\neq -c$ the other two cubic terms in Eq. (2.4) may be used to study the difference between potential and nonpotential evolutions.

A second class of model equations,

$$\partial_t\psi=[r-(\nabla^2+1)^2]\psi+d\nabla^2\psi(\nabla\psi)^2 +(3-d)(\partial_i\psi)(\partial_j\psi)\partial_i\partial_j\psi\ , \tag{2.5}$$

is suggested by the work of Gertsberg and Sivashinsky on Rayleigh-Bénard convection between poorly conducting upper and lower plates.[14] Here the parameter r, as before, can be considered a reduced Rayleigh number while the parameter d provides a convenient way to interpolate between potential ($d=1$) and nonpotential ($d\neq 1$) equations. For poorly conducting horizontal boundaries, the wavelength of the spatially periodic solution at threshold diverges as the ratio of the conductivity of the plates to the conductivity of the fluid tends to zero. This allows a direct slow-gradient expansion of the hydrodynamic equa-

tions, which Gertsberg and Sivashinsky developed in one horizontal dimension.

Our motivation for also studying Eq. (2.5) is that the structure of the nonlinear term for locally one-dimensional solutions is derived directly from the hydrodynamic equations, albeit in a situation rather different from the usual circumstances. In addition, since their expansion parameter is $\epsilon \sim b^{1/2}(1-r)^{-1/2}$ with b small (see Ref. 14), the derivation of the Gerstberg-Sivashinsky equation is not restricted to the weakly nonlinear region $r \ll 1$. Thus Eq. (2.5) may describe the basic features of the convecting roll solution, especially the structure of the nonlinearities, more successfully than the lowest-order truncation leading to Eq. (2.1).

We remark in passing that the correct *two*-dimensional equation describing convection between thin poor conductors is given by $d=1$ in Eq. (2.5), which leads to a potential equation. This can be seen from the work of Busse and Riahi[15] or the later direct calculation by Pismen.[16] Also the case $d=0$ applies to experiments with thick plates if the heat flow and Rayleigh number are controlled to eliminate the nonlocal nonlinear term calculated in the work of Busse and Riahi. Both these equations lead to square cell solutions as the stable pattern and so are not useful to our present purpose. The stability of such solutions will be discussed elsewhere.[17]

Both Eqs. (2.1) and (2.5) may be further generalized by adding terms which model the coupling to vertical vorticity.[8] This coupling has been suggested to play a key role in the onset of turbulence; the skewed-varicose instability, in particular, depends crucially on the introduction of such terms.[18] We thus consider models for which the left side is modified to include an additional advection by a solenoidal drift velocity $\mathbf{U}$,

$$\partial_t \psi \rightarrow \partial_t \psi + (\mathbf{U}\cdot\nabla)\psi \ . \tag{2.6}$$

The drift velocity $\mathbf{U}$ is defined in terms of the vertical vorticity potential $\zeta(x,y,t)$:

$$\mathbf{U}=(U_x,U_y)=(\partial_y\zeta,-\partial_x\zeta) \ , \tag{2.7}$$

where

$$\nabla^2\zeta = g\nabla(\nabla^2\psi)\times\nabla\psi\cdot\hat{\mathbf{z}} \ , \tag{2.8}$$

and g is a non-negative coupling constant. Note that $-\nabla^2\zeta$ is simply the vertical component of the fluid vorticity.

Equations (2.6) and (2.8) are the natural extension to a rotationally invariant form of the conjecture of Siggia and Zippeluis for rigid boundaries.[8] For small r, Eqs. (2.6)—(2.8) reduce in perturbation theory to their expression and also to the more general calculation by Cross and Newell for rigid boundaries.[4] Similar equations have been proposed by Manneville[9] and also by Pismen[16] for convection between poor conductors. Note that Eq. (2.8) neglects the intrinsic dynamics of the vorticity field (there is no time derivative of ζ). As a result, the imaginary part of the growth rate of any instability will be zero and only soft-mode instabilities will occur. The hard-mode oscillatory instability of Busse is not contained in our equations. It could be incorporated by replacing $\nabla^2\zeta$ by $(\nabla^2+c-\partial_t)\nabla^2\zeta$ in Eq. (2.8) with c an $O(1)$ constant, but we have not investigated such a modification.

The parameter g in Eq. (2.8) defines the strength of the singular mean drift effects relative to the nonsingular nonlinear terms. We expect that large g will correspond to small Prandtl numbers. This is indeed consistent with the behavior we find below for the variation of the stability boundaries with g.

These stability boundaries also show that the simple form of Eqs. (2.6)—(2.8) in fact is *not* adequate; we find that these equations have short-wavelength contributions to the vorticity flow that in turn enhance short-wavelength instabilities (such as the cross-roll instability). These then preempt the long-wavelength instabilities that are our main concern. Although we believe that such short-wavelength flows do exist in the real fluid equations, parametrizing both long- and short-wavelength components in terms of the single parameter g turns out to be too crude to balance their effects properly. We thus introduce a filtering operator that reduces the amplitude of the short-wavelength components. For simplicity we choose a Gaussian,

$$F_\gamma[f(x,y)]=(4\pi\gamma^2)^{-1}\int dx'\,dy'\,f(x',y')\exp\left[\frac{-(x-x')^2+(y-y')^2}{4\gamma^2}\right] . \tag{2.9}$$

In Fourier space, the effect of F_γ is to reduce the amplitude of a Fourier component with wave number q by $\exp(-\gamma^2q^2)$. For $\gamma \gtrsim 2$ the filter effectively eliminates any components at the roll wavelength or shorter while leaving the long-wavelength components unchanged. We then replace Eq. (2.8) by

$$\nabla^2\zeta = gF_\gamma[\nabla(\nabla^2\psi)\times\nabla\psi\cdot\hat{\mathbf{z}}] \ . \tag{2.10}$$

For numerical simulations, these equations need to be supplemented with boundary conditions for ψ and ζ. Periodic boundary conditions are the simplest to implement but fail to include the effect of rigid lateral walls or, in the case of rectangular cells, of corners. The experimentally relevant, rigid boundary conditions for ψ should remain unchanged when vorticity is included. They are[13]

$$\partial_n\psi=(\hat{\mathbf{n}}\cdot\nabla)\psi=0 \ , \tag{2.11}$$

where $\hat{\mathbf{n}}$ is the normal to the boundary. The natural boundary condition on the drift velocity would be $\mathbf{U}=\mathbf{0}$ on all boundaries. However this results in too many constraints for Eq. (2.10) which has only second-order spatial derivatives on the left side. This problem arises because of the reduction in the order of the horizontal differential operator used on the left-hand side. Solutions which are

localized near the walls and decay in an $O(1)$ length scale from the wall are thereby eliminated. It is then clear, in analogy to the derivation of the boundary conditions on the complex amplitude function,[19] that the boundary condition

$$\zeta=0 \tag{2.12}$$

(i.e., $\hat{\mathbf{n}}\cdot\mathbf{U}=0$) is sufficient for the slowly varying component of the vorticity potential. The nonzero tangential component of the drift velocity $(\hat{\mathbf{n}}\cdot\nabla)\zeta$ would, in a real fluid cell, then decay to zero on an $O(1)$ length scale. This should not give important differences in a large cell.

In summary we have defined a large class of models that are more general than the Swift-Hohenberg model. The nonlinear term there has been changed to eliminate the potential nature of the dynamics and to allow more flexibility in adjusting the wave-number dependence of the stability boundaries. In addition we have included a coupling to a vorticity field that is driven by inhomogeneities in the periodicity of the field. This incorporates in a physically sensible way the singular nature of the gradient expansion for slow changes to a periodic state. We summarize the models in Table I. They are much simpler than the full fluid equations and are more tractable for both analytic and numerical work.

III. STABILITY ANALYSIS

If we consider the stability of the straight-roll solutions with respect to a restricted class of perturbations, namely, those of long wavelength, significant analytic progress can be made before resorting to numerical work. This is a useful complement to the direct Galerkin analysis discussed below, since that approach can become delicate in the search for long-wavelength instabilities. In addition we remark that for the model equations that we have investigated, it is usually a good approximation to use a single-mode truncation of the unperturbed solution, over most of the range $0<r<1$ on which we have concentrated our study. This makes it easy to derive approximate algebraic expressions $r(K)$ for the long-wavelength stability boundaries, providing a rapid way to analyze new models.

TABLE I. Two-dimensional models of three-dimensional convection.

Model I

$$\partial_t\psi+(\mathbf{U}\cdot\nabla)\psi=[r-(\nabla^2+1)^2]\psi-a\psi^3-b\psi(\nabla\psi)^2+c\psi\nabla^2\psi$$

Model II

$$\partial_t\psi+(\mathbf{U}\cdot\nabla)\psi=[r-(\nabla^2+1)^2]\psi+d(\nabla\psi)^2\nabla^2\psi+(3-d)(\partial_i\psi)(\partial_j\psi)\partial_i\partial_j\psi$$

where

$$\mathbf{U}=(\partial_y\xi,-\partial_x\xi)$$

$$\nabla^2\xi=gF_\gamma[\nabla(\nabla^2\psi)\times\nabla\psi\cdot\hat{\mathbf{z}}]$$

$$F_\gamma(\psi)=(4\pi\gamma^2)^{-1}\int dx'\,dy'\,\psi(x',y')\exp\left[\frac{-(x-x')^2-(y-y')^2}{4\gamma^2}\right]$$

Boundary conditions for finite cells: $\psi=\partial_n\psi=\zeta=0$

The long-wavelength instabilities are contained in the phase-diffusion equation introduced by Pomeau and Manneville[20] to study small perturbations to straight rolls with wave vector $\mathbf{K}=(K,0)$:

$$\tau\partial_t\theta=D_{||}(K)\partial_x^2\theta+D_\perp(K)\partial_y^2\theta\ . \tag{3.1}$$

Here θ is a phase variable such that the field variable is locally periodic in θ with period 2π. Then the wave vector is given by

$$\mathbf{K}=\nabla\theta\ . \tag{3.2}$$

The straight-roll pattern at wave number K is stable to long-wavelength perturbations for positive diffusion constants $D_{||}(K)$ and $D_\perp(K)$. An instability is signaled by $D_{||}$ (Eckhaus) or $D_\perp$ (zigzag) passing through zero.

The addition of the vorticity coupling to the models leads to the modified diffusion equation

$$\tau\partial_t\theta=D_{||}\partial_x^2\theta+(D_\perp+\alpha)\partial_y^2\theta+\beta(\partial_x^2+\partial_y^2)^{-1}\partial_x^2\partial_y^2\theta\ , \tag{3.3}$$

with τ, $D_{||}$, and $D_\perp$ as before. Values for α and β for the various models are derived in the Appendix.

For a perturbation of wave vector $\mathbf{k}=k(\cos\phi,\sin\phi)$, the growth rate λ is given by

$$-\frac{\lambda}{k^2}=D_{||}\cos^2\phi+(D_\perp+\alpha+\beta\cos^2\phi)\sin^2\phi\ . \tag{3.4}$$

Since $\alpha>0$, vorticity acts as a stabilizing influence on the zigzag instability ($\phi=\pi/2$). However, for the ranges of r and k for which β is negative, a new instability develops at an intermediate angle; this instability may be identified as the skewed-varicose instability. It is straightforward to find analytically the value ϕ^* maximizing the growth rate λ in Eq. (3.4).

Only long-wavelength instabilities are given by this phase-diffusion approach. A complete stability analysis that includes short-wavelength instabilities must be calculated by numerical methods from the original equations. We used a Galerkin method similar to that used by Busse and Clever,[5] but much simpler since the z dependence of all fields in the model equations has been eliminated. (The technique is also briefly explained in Greenside and Coughran,[12] who calculated the stability boundaries of the Swift-Hohenberg model.) A numerical Galerkin method yields the maximum eigenvalue for an eigenfunction of a particular symmetry, on a discrete mesh of points in the "control-parameter"—wave-number plane. Interpolating between values of wave number where the eigenvalue changes sign yields an approximation to the stability boundary for an instability of known symmetry. For the two-dimensional model equations of interest, the numerical problem of calculating stability boundaries is essentially trivial and high accuracy can be achieved. The only difficulty arises when distinct instabilities, such as the long-wavelength zigzag and short-wavelength cross roll, have the same symmetry in which case the straightforward numerical method can change stability branches and yield incorrect boundaries (Fig. 1). The analytical long-wavelength boundaries calculated above turned out to be crucial in interpreting and understanding the numerical

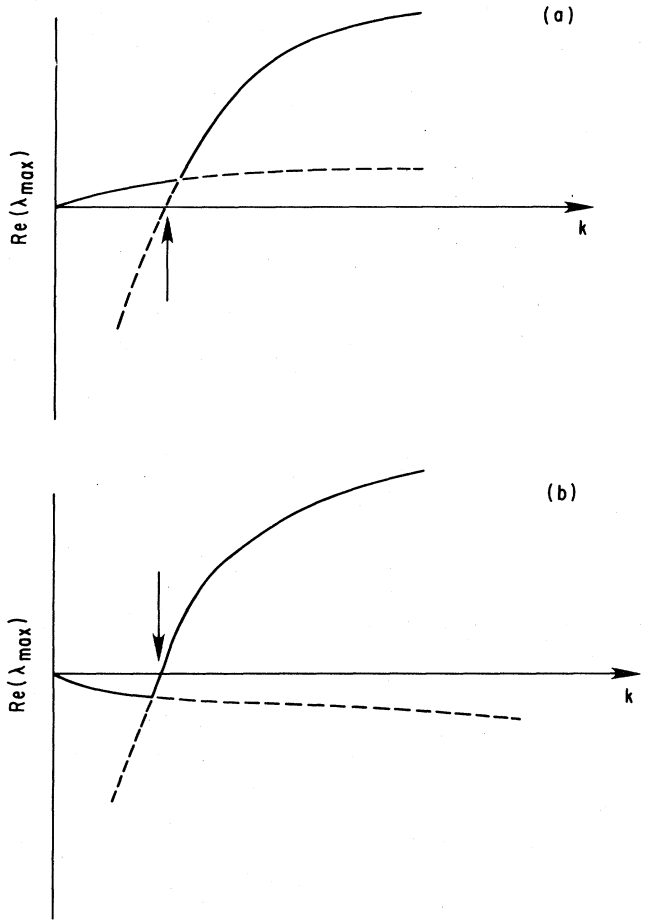

FIG. 1. Schematic example of numerical difficulties in finding a stability boundary, i.e., a zero crossing of $\mathrm{Re}(\lambda_{\max})$ where $\lambda_{\max}$ is the growth rate with the largest real part for an eigenfunction of given symmetry. (a) As the roll wave number k_x is varied, an unstable long-wavelength branch changes over to a short-wavelength branch, hiding the zero crossing of the latter (shown by an arrow). The short-wavelength instability may be missed. (b) An unstable short-wavelength branch crosses a stable long-wavelength branch: a zero crossing of the latter (also indicated by an arrow) may be incorrectly deduced. In both cases, the kinks in $\mathrm{Re}(\lambda_{\max})$ do not allow zero-finding algorithms that use derivatives.

results, especially for small roll wave numbers K for which many eigenvalues of different symmetry become positive at the same time.

The properties of the four instabilities that occur for our model equations are summarized in Table II. These instabilities are similar to the ones studied for the Boussinesq equations by Busse and Clever.

IV. RESULTS

We have analyzed a number of models representative of classes I and II (see Table I). We will first discuss a particular model that most successfully reproduces the stability diagram near onset of the Boussinesq equations. The direct simulation of this model in a finite geometry should provide useful insights. We then describe our experience with other choices of the models.

A model that qualitatively reproduces the fluid stability diagram is an example of model II ($d=3$); the complete equations are

$$\begin{aligned}&\partial_t\psi+\mathbf{U}\cdot\nabla\psi=[r-(\nabla^2+1)^2]\psi+3\nabla^2\psi(\nabla\psi)^2\,,\\&\mathbf{U}=(U_x,U_y)=(\partial_y\zeta,-\partial_x\zeta)\,,\\&\nabla^2\zeta=gF_\gamma[\nabla(\nabla^2\psi)\times\nabla\psi\cdot\hat{\mathbf{z}}]\,,\end{aligned}\tag{4.1}$$

where the short-wavelength components of ζ are eliminated using the filter F_γ, Eq. (2.9), for $\gamma\gtrsim 2$.

First, we show in Fig. 2 the stability diagram for no vorticity coupling, $g=0$. For values of the control parameter $r<1$, there is an interval of wave numbers $K_-(r)<K<K_+(r)$ in which the periodic solutions are stable to all small perturbations. The stable region is bounded by the longitudinal long-wavelength Eckhaus instability on the upper side K_+, and for $r<0.65$, by the purely transverse long-wavelength zigzag instability on the lower side K_-. The only other new instability appearing in the diagram is the short-wavelength cross-roll instability, where the perturbation eigenfunction corresponds to a new set of rolls, always orthogonal to the existing set. For $r>0.6$ and $K<0.45$, the model is complicated by the existence of and transitions between multiple solutions. The new solutions grow out of the (r,K) points where K and nK, $n=3$, 5, etc., are *both* marginally stable (the even n solutions do not connect to the basic solution). Approaching the point $(r=1,K=0)$, more and more of these

TABLE II. Instabilities of rolls for models I and II.

Name	Character	Perturbation wave vector $\mathbf{k}=(k_x,k_y)$	Comments
Cross roll (knot)	short wavelength	$k_x=0,\ k_y=O(1)$	Only short-wavelength instability
Zigzag	long wavelength	$k_x=0,\ 0<k_x\ll 1$	Curve for which $D_\perp=0$
Eckhaus	long wavelength	$0<k_y\ll 1,\ k_y=0$	Independent of g, curve for which $D_{\|\|}=0$
Skewed varicose	long wavelength	$0<k_x,k_y\ll 1,\ k_y/k_x$ finite	Occurs only for $g\neq 0$

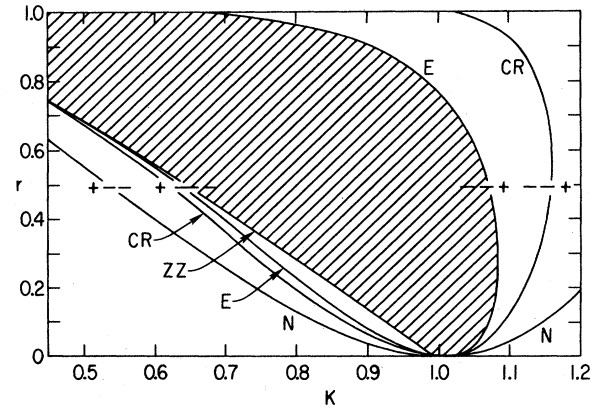

FIG. 2. Stability boundaries for model II ($g=0$, $d=3$), as a function of the roll wave number K and the control parameter r. The labels N, E, ZZ, and CR refer to the neutral, Eckhaus, zigzag, and cross-roll instabilities. There is no skewed-varicose instability (denoted SV in later figures). The plus and minus signs on either side of a stability boundary show where λ_{max} is positive or negative. The region of wave numbers stable to all perturbations is shaded. The accuracy of the calculation is ± 0.002 in K for a given value or r.

solutions are found with some overlapping of existence regions. Cleary the neighborhood of this special point is highly singular; we will not discuss it further here.

In Fig. 3, we show the stability diagram with the addition of the vorticity coupling with the long-wavelength filtering $\gamma=2$ and for an intermediate value of $g=10$. The vorticity has two effects. Firstly, the zigzag instability is suppressed, so that it no longer forms the lower stability boundary in Fig. 3 except for very small r. Secondly, a new long-wavelength instability appears with wave vector neither entirely transverse nor longitudinal to the original wave vector; this is the skewed-varicose instability. Both these trends for increasing g follow the trends in the Boussinesq stability diagram with decreasing Prandtl number. Note also that Fig. 3 shows a stability interval

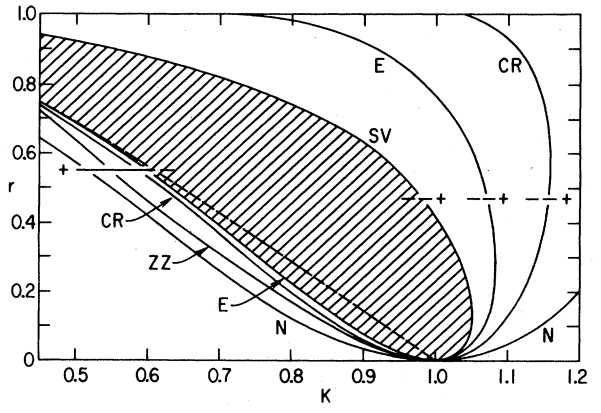

FIG. 3. Stability boundaries for model II ($d=3$) for $g=10$ with the Gaussian filter on the vorticity equations (2.9) and (2.10) with $\gamma \geq 2$. The dashed line is the wave number selected in axisymmetric convection.

$K_-(r) < K < K_+(r)$ that tends towards decreasing wave number with increasing r, so that the critical wave number becomes unstable to the skewed-varicose instability at some value of r. [The trend towards decreasing wave number K is clearly a result of the decreasing strength of the nonlinear saturating term in Eq. (4.1) with decreasing K, which is also present in the full fluid equations. In the model equation, in fact, the $K=0$ mode grows without bound for $r>1$, consistent with the cutoff in the diagram at this point.] In addition, on Fig. 3 we plot the path of the zigzag instability for no vorticity coupling $g=0$. This is the wave number selected at large distances in axisymmetric convection, independent of g since vorticity is not driven in this symmetry. This wave number may be important in more general situations where there are focus singularities in the pattern.[4] Note that this line does *not* intersect the skewed-varicose instability boundary in this model. It is not known whether these lines intersect for the fluid equations, an important issue which has not yet been settled by calculation.

The model equation is sufficiently simple that it is easy to study in detail the properties of the skewed-varicose instability. In particular, we find that it grows *continuously* out of the Eckhaus instability both for increasing g and increasing r; for finite g and r, the Eckhaus instability is the limit of the range of skewed-varicose instability for $k_y/k_x \to 0$. These remarks should also apply to the full fluid equations. In Fig. 4 we show the variation with r of $\phi^* = \tan^{-1}(k_y/k_x)$ for the skewed-varicose boundary (i.e., for the most unstable perturbation) for $g=10$. As $r \to 0$, we find analytically that ϕ^* approaches a constant value $\phi_0^* = 59°$ for this value of g, with $\phi_0^* - \phi(r) \sim r^{1/4}$.

We have also studied this model for the vorticity coupling without the filtering F_γ for $g=10$ in Fig. 5. The long-wavelength boundaries are, of course, unchanged. However the short-wavelength cross-roll instability on the large K side is dramatically enhanced by the short-length-scale vorticity flows; it preempts the skewed-varicose instability for most values of r. In fact for $r \gtrsim 0.65$, no stable stationary singly periodic solutions exist. We believe that the enhancement of the cross-roll instability by the vorticity is a real effect and that the instability becomes the knot instability of Busse and Clever.

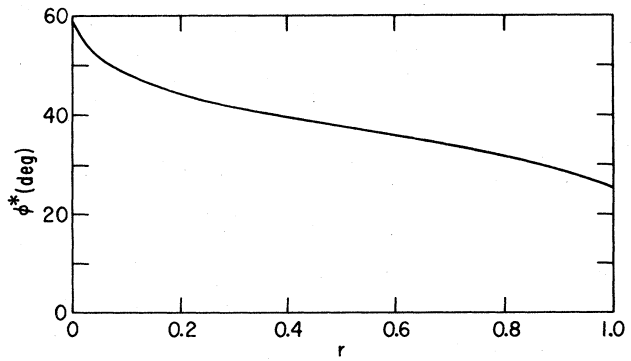

FIG. 4. The r dependence of the perturbation angle $\phi^* = \tan^{-1}(k_y/k_x)$ which maximizes the growth rate λ for the skewed-varicose instability of model II, when $g=10$ (Fig. 3).

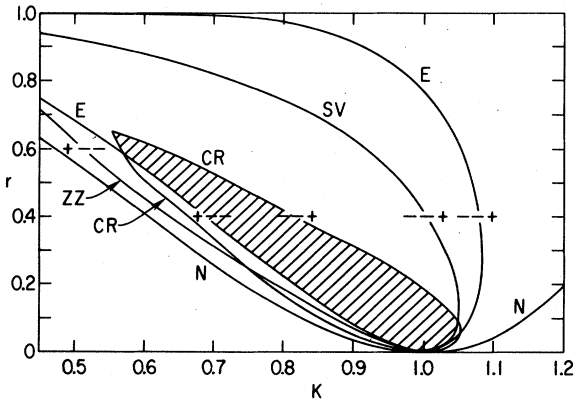

FIG. 5. Stability boundaries for model II ($d=3$) for $g=10$ and no Gaussian filter ($\gamma=0$).

These authors found a delicate competition between the knot and skewed-varicose instabilities for low and moderate Prandtl numbers. Our parametrization of the vorticity at both long and short length scales by a single parameter g does not give this delicate balance correctly. We have therefore suggested the filtering F_γ to suppress the short-wavelength effects and to allow the long-wavelength effects that are our main interest to play a dominant role.

To complete the stability picture of the model, we show in Fig. 6 the variation of the boundaries with vorticity coupling for fixed r (we used the value $r=0.3$). Again if the unfiltered vorticity is used, the short-wavelength cross-roll instability on the high K side is enhanced: it preempts the skewed-varicose instability for $g>7$ and leaves no stable singly periodic solution for $g>25$ for this value of r.

We now discuss the stability for other choices of the constants. For model II, as the parameter d changes, the long-wavelength instabilities remain qualitatively unchanged (the Eckhaus instability is independent of d). However as d decreases, the cross-roll instability is enhanced, and for $d<\frac{3}{2}$ there are no stable singly periodic solutions remaining even in the absence of vorticity coupling. We have shown that rectangular cell solutions are stable in this region, as found for convection between poor conductors. A complete stability analysis of these solutions will be presented elsewhere.[17]

The stability diagram of the Swift-Hohenberg equation (model I, $a=1$, $b=c=0$) is shown in Fig. 7. The stability interval is bounded on the low wave-number side by the zigzag instability. The stable interval grows with increasing r, and there is no interesting r-dependent wave-number selection.

The effect of including vorticity is shown in Fig. 8 for $g=25$. The zigzag instability is suppressed, so that it no longer bounds the stable region except for small r, and the skewed-varicose instability is enhanced. The skewed-varicose instability boundary has positive slope and does not play a role in forcing the wave number to smaller values in this model. If the long-wavelength filtering is not employed, the cross-roll instability on the high wave-number side is again enhanced and preempts the skewed-varicose instability for most values of r as shown. For still larger g (~ 100), this instability eliminates the stable solutions except *very* close to threshold ($r\sim 1/g$) and for $r>0.3$. In Fig. 9 we show the dependence of the stability boundaries on g for a fixed value of $r=0.3$. This figure shows clearly how the short-wavelength cross-roll instability depends sensitively on the coupling to vorticity.

Although we have not explored the full parameter space of coefficients a, b, and c in model I, calculations similar

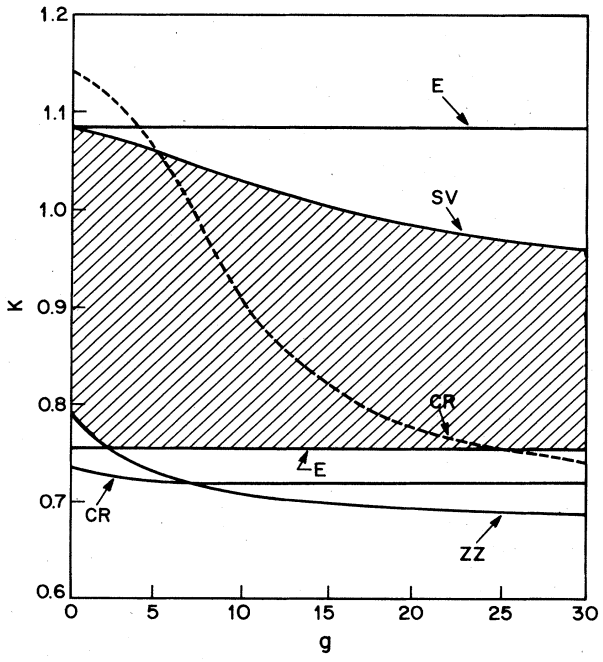

FIG. 6. The g dependence of the positions of the instability boundaries for model II ($d=3$), with $r=0.3$. The shaded region is stable for the model with Gaussian filtering ($\gamma=2$). The dashed line denotes the cross-roll unstability with *no* Gaussian filtering and further limits the stable region in this case.

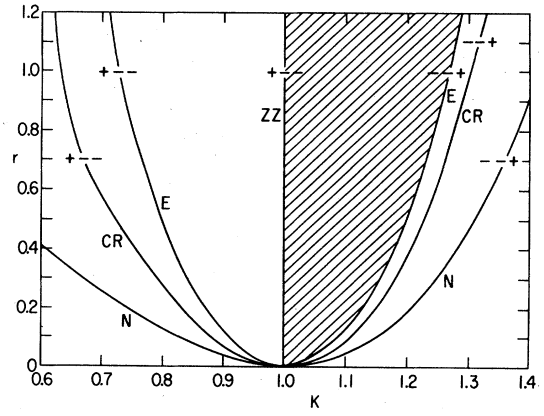

FIG. 7. Stability boundaries of the Swift-Hohenberg model (model I with $g=0$, $a=1$, $b=c=0$).

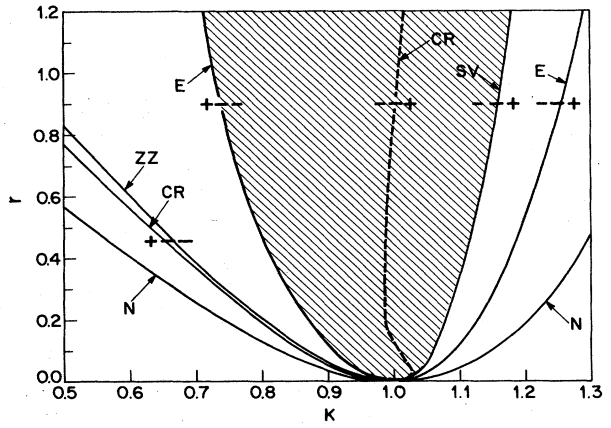

FIG. 8. Stability boundaries of the Swift-Hohenberg model for $g=25$. The shading shows the stable region employing the Gaussian filter, Eq. (2.9), with $\gamma=2$. In this case the CR line is not displaced from that in Fig. 7. The dashed line is the CR boundary without using a Gaussian filter ($\gamma=0$).

to those described above on several different choices of these parameters give results qualitatively similar to those described for the Swift-Hohenberg model with vorticity. In particular, no combination of these coefficients were found which avoided the preemption of the skewed-varicose instability by the knot instability, which gave a skewed-varicose stability boundary that bounded the region of stable wave numbers, as shown in Fig. 3, or for which the preferred wave number intersected the skewed-varicose instability boundary.

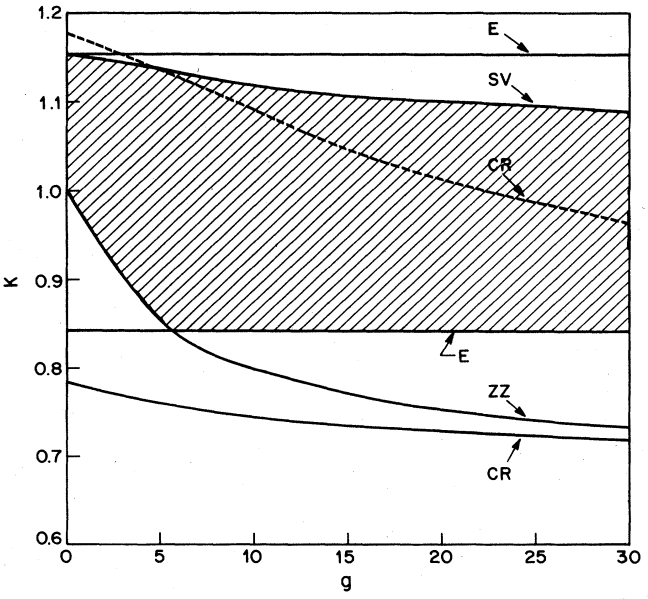

FIG. 9. The g dependence of the positions of the instability boundaries for the Swift-Hohenberg model ($a=1$, $b=c=0$), calculated for $r=0.3$. Again the shading shows the stable region with Gaussian filtering ($\gamma=2$), for which the CR values become independent of g.

V. CONCLUSIONS

The linear-stability diagrams of straight-roll patterns in Sec. IV provide a first analysis of various model equations. Direct numerical simulations may now be performed to investigate the dynamical behavior of the models and to compare them with the real fluid systems.

For example, in analogy to the experiments of Busse and Whitehead,[21] one can numerically set up an initial condition of parallel rolls in a system with periodic boundary conditions and investigate the evolution following the various instabilities. The stability analysis predicts the initial linear growth of a perturbation to the pattern, but says nothing about the later time evolution, such as whether the system settles down at a new wave number within the stability region, or evolves continuously in time without reaching a new steady state. This numerical experiment may be particularly interesting in comparing the behavior following the Eckhaus instability and following the skewed-varicose instability. One could easily believe that a longitudinal instability (Eckhaus) may simply result in the addition or subtraction of rolls. On the other hand, one might speculate that the skewed-varicose instability, leading to a more complicated two-dimensional distortion, may lead to a continually evolving state. Model II with $d=3$ is particularly convenient for this comparison: for no vorticity coupling ($g=0$), increasing the control parameter at fixed wave number leads to the Eckhaus instability, whereas for $g\neq 0$, the skewed-varicose instability is encountered first.

The same model (particularly with the Gaussian filtering of the vorticity) seems to reproduce qualitatively the behavior of the original equations. Thus it seems that the natural extensions of the models to include vorticity produce equations in which the short-wavelength cross-roll instability becomes too prominent a feature. It may be remarked that the cross-roll instability in fluids is enhanced at low Prandtl numbers (becoming the "knot" instability), a feature reproduced by the model equations, and that the competition between knot and skewed-varicose instabilities is a delicate one. The simple vorticity coupling, Eqs. (2.6)—(2.8), tips the balance too strongly towards the knot so that the filtering procedure is needed for the skewed-varicose instability to bound the stable region.

A further use of these model equations is to test general ideas such as wave-number selection. In particular the experimental configurations used to investigate various wave-number selection processes[22,23] (a single dislocation, a grain boundary, axisymmetric convention) may be simulated. These experiments led to the conclusion that a *common* wave number was selected by these different processes, a result not expected from theoretical analysis. Work to investigate this question on the general model equations discussed here is currently in progress.

APPENDIX: DERIVATION OF THE EXPRESSIONS FOR THE DIFFUSION CONSTANTS

For simplicity, we develop the method for model I with $a=1$, $b=c=0$:

$$\partial_t\psi = r\psi - (\nabla^2+1)^2\psi - \psi^3 . \tag{A1}$$

The reader may readily repeat the algebra for the other models. For more details of the formalism see Ref. 4.

To incorporate the slow variation of the periodic pattern introduced by the long-wavelength perturbation, we introduce slow space and time variables

$$X=\eta^2 x, \quad Y=\eta^2 y, \quad T=\eta^4 t \tag{A2}$$

and a scaled phase variable Θ:

$$\theta(x,y,t)=\eta^{-2}\Theta(X,Y,T) . \tag{A3}$$

The derivatives of Θ with respect to its arguments (the scaled variables) are $O(1)$. Thus the local wave vector is

$$\mathbf{K}(X,Y,T)=\nabla_{\mathbf{x}}\theta=\nabla_X\Theta . \tag{A4}$$

We assume $\eta^2 \ll 1$ and develop the solution as an expansion in η^2:

$$\psi=\psi^{(0)}(\theta,X,Y,T)+\sum_{p=1}^{\infty}\eta^{2p}\psi^{(p)}(\theta,X,Y,T) , \tag{A5}$$

where $\psi^{(i)}$ are periodic in the phase θ with period 2π. The solution is obtained by expanding (A1) in power of η^2 using

$$\nabla f(\theta,X,Y,T)=\mathbf{K}\partial_\theta f+\eta^2\nabla_{\mathbf{X}} f , \tag{A6}$$

where $\nabla_{\mathbf{X}}=(\partial/\partial X,\partial/\partial Y)$ denotes the gradient with respect to the slow variables. Then we find

$$\nabla^2 f(\theta,X,Y,T)=[K^2\partial_\theta^2+\eta^2 D_1+\eta^4(\partial_X^2+\partial_Y^2)]f \tag{A7}$$

with

$$D_1=2\mathbf{K}\cdot\nabla_{\mathbf{X}}+(\nabla_{\mathbf{X}}\cdot\mathbf{K}) . \tag{A8}$$

At zeroth order we obtain the equation giving $\psi^{(0)}=\psi_0$, the unperturbed solution

$$0=\hat{O}\psi_0=r\psi_0-(K^2\partial_\theta^2+1)^2\psi_0-\psi_0^3 . \tag{A9}$$

At $O(\eta^2)$ the equation takes the form

$$\delta\hat{O}\psi^{(1)}=F^{(1)} , \tag{A10}$$

where $\delta\hat{O}$ is the linearization of the operator $\hat{O}$ about the unperturbed solution

$$\delta\hat{O}=r-(K^2\partial_\theta^2+1)^2-3\psi_0^2 \tag{A11}$$

and $F^{(1)}$ contains all terms of $O(\eta^2)$ involving only ψ_0, $\mathbf{K}$, and their derivatives

$$F^{(1)}=(K^2\partial_\theta^2+1)D_1\partial_\theta\psi_0+D_1(K^2\partial_\theta^2+1)\partial_\theta\psi_0-\Theta_T(\partial_\theta\psi_0) , \tag{A12}$$

where $\Theta_T=\partial_T\Theta$. The phase-diffusion equation arises as the solubility condition removing secular terms for $F^{(1)}$, namely, that $F^{(1)}$ contains no component in the null space of $\delta\hat{O}$. For a self-adjoint operator $\hat{O}$ this simply requires

$$\langle(\partial_\theta\psi_0),F^{(1)}\rangle=0 \tag{A13}$$

with $\partial_\theta\psi_0$ the zero eigenvalue translation mode and where $\langle\ ,\ \rangle$ denotes the scalar product

$$\langle a,b\rangle=\frac{1}{2\pi}\int_0^{2\pi}d\theta\, ab=\langle ab\rangle . \tag{A14}$$

For Eq. (A1) this leads to the explicit equations quoted in the text.

For non-self-adjoint operators $\hat{O}$, such as those appearing in model II, the procedure is more complicated. The solubility condition takes the form

$$\langle e_0^+,F^{(1)}\rangle=0 , \tag{A15}$$

where e_0^+ is the zero-eigenvalue periodic eigenvector of the adjoint $\delta\hat{O}^+$ to $\delta\hat{O}$. In general e_0^+ is not simply related to the unperturbed solution to $\hat{O}$ and must be solved for independently. It is easy to see, however, that if the Fourier expansions of the solutions are truncated to one mode as discussed in the text, then e_0^+ is simply constructed:

$$\psi_0\simeq A\cos\theta, \quad e_0^+\simeq\sin\theta . \tag{A16}$$

The expressions for model II with this approximation are quoted in the text. We have not pursued the calculation for this model beyond the one-mode approximation at present. Note that although model II is generally not potential, the operators $\hat{O}$ and $\delta\hat{O}$ defined for this model are self-adjoint with the simple scalar product (A14).

The calculation of the vorticity correction induced by the coupling introduced in Sec. II is straightforward. For slowly varying perturbations, the only contribution to the drift $\mathbf{U}$ at $O(\eta^2)$ is the uniform part $\mathbf{U}$ (i.e., with no dependence on the fast scale θ). Then adding the vorticity correction to $F^{(1)}$ in Eq. (A12) leads to the change

$$\delta F^{(1)}=-\mathbf{K}\cdot\mathbf{U}(\partial_\theta\psi_0) , \tag{A17}$$

showing immediately that at this order the vorticity leads simply to an extra convection of the phase field

$$\delta\Theta_T=-\mathbf{K}\cdot\mathbf{U} . \tag{A18}$$

It is a matter of straightforward substitution to show that the θ-independent component of Eq. (2.10) reduces to

$$(\partial_X^2+\partial_Y^2)\delta^{(1)}=-q\hat{\mathbf{z}}\cdot\mathbf{K}\times\nabla_X[\nabla_X\cdot\mathbf{K}\langle(\partial_\theta\psi_0)^2\rangle] . \tag{A19}$$

Finally, linearizing in small derivations from a simply periodic pattern leads to the phase Eq. (3.3) quoted in the text. We now quote the results for the models, first in complete generality in terms of the fully nonlinear unperturbed solution ψ, and then with the one-mode truncation

$$\psi_0\simeq A\cos\theta, \quad \theta=\mathbf{K}\cdot\mathbf{x}$$

with A determined from the equation for ψ by taking the scalar product with $\cos\theta$.

Model I with $a=1$, $b=c=0$:

$$D_\perp(K)=2\langle K^2(\partial_\theta^2\psi_0)^2-(\partial_\theta\psi_0)^2\rangle\simeq(K^2-1)A^2 , \tag{A20}$$

$$D_{||}(K)=\frac{d}{dK}[KD_\perp(K)] , \tag{A21}$$

$$\tau(K)=\langle(\partial_\theta\psi_0)^2\rangle\simeq\tfrac{1}{2}A^2 , \tag{A22}$$

with

$$A^2=\tfrac{4}{3}[r-(K^2-1)^2]\ . \tag{A23}$$

In these expressions $\langle\ \rangle$ denotes an average over one wavelength.

Model I, general case. For arbitrary a, b, and c we have analytic results only for the one-mode approximation

$$D_\perp(K)\simeq(K^2-1)A^2+\tfrac{1}{8}bA^4\ , \tag{A24}$$

$$D_{||}(K)\simeq\frac{d}{dK}[K(K^2-1)A^2]+\tfrac{1}{16}(b-c)K\frac{d}{dK}A^4+\tfrac{1}{8}bA^4\ , \tag{A25}$$

$$\tau(K)\simeq\tfrac{1}{2}A^2\ , \tag{A26}$$

with

$$A^2=(\tfrac{3}{4}a+\tfrac{3}{8}bK^2+\tfrac{1}{8}cK^2)^{-1}[r-(K^2-1)^2]\ . \tag{A27}$$

Model II:

$$D_\perp(K)=2\langle K^2(\partial_\theta^2\psi_0)^2-(\partial_\theta\psi_0)^2\rangle+dK^4\langle(\partial_\theta\psi_0)^4\rangle$$
$$\simeq(K^2-1)A^2+\tfrac{3}{8}dK^4A^4\ , \tag{A28}$$

$$D_{||}(K)=\frac{d}{dK}[KD_\perp(K,d=1)]\ , \tag{A29}$$

$$\tau(K)=\langle(\partial_\theta\psi_0)^2\rangle\simeq\tfrac{1}{2}A^2\ , \tag{A30}$$

with

$$A^2=\tfrac{4}{3}[r-(K^2-1)^2]\ . \tag{A31}$$

The potential model IIA is given by $d=1$. The parameters α and β giving the modifications on adding the vorticity coupling as defined in Eq. (3.3) are given by

$$\frac{\alpha}{\tau}=gK^2\langle(\partial_\theta\psi_0)^2\rangle\simeq\tfrac{1}{2}gK^2A^2\ . \tag{A32}$$

$$\frac{\beta}{\tau}=gK^3\frac{d}{dK}\langle(\partial_\theta\psi_0)^2\rangle\simeq\tfrac{1}{2}gK^3\frac{d}{dK}A^2\ . \tag{A33}$$

---

[1]F. H. Busse, Rep. Prog. Phys. **41**, 1929 (1978).

[2]J. P. Gollub, A. R. McCarriar, and J. F. Steinman, J. Fluid Mech. **125**, 259 (1982).

[3]G. Ahlers and R. P. Behringer, Prog. Theor. Phys. Suppl. **64**, 186 (1979).

[4]M. C. Cross and A. C. Newell, Physica (Utrecht) **10D**, 299 (1984).

[5]F. H. Busse and R. M. Clever, J. Fluid Mech. **91**, 319 (1979).

[6]A. C. Newell and J. A. Whitehead, J. Fluid Mech. **38**, 279 (1969).

[7]L. A. Segel, J. Fluid Mech. **38**, 203 (1969).

[8]E. D. Siggia and A. Zippelius, Phys. Rev. Lett. **47**, 835 (1981); A. Zippelius and E. D. Siggia, Phys. Fluids **16**, 2905 (1983).

[9]P. Manneville, J. Phys. (Paris) **44**, 759 (1983).

[10]J. Swift and P. C. Hohenberg, Phys. Rev. A **15**, 319 (1977).

[11]M. C. Cross, Phys. Fluids **23**, 1727 (1980).

[12]H. S. Greenside, W. M. Coughran, Jr., and N. L. Schryer, Phys. Rev. Lett. **49**, 726 (1982); H. S. Greenside and W. M. Coughran, Jr., Phys. Rev. A **30**, 398 (1984).

[13]M. C. Cross, Phys. Rev. A **25**, 1065 (1982).

[14]V. L. Gertsberg and G. I. Sivashinsky, Prog. Theor. Phys. **66**, 1219 (1981). Equation (2.5) is the most general rotationally invariant two-dimensional equation consistent with the one-dimensional calculation of Gertsberg and Sivashinsky. These authors derive an expression for the parameter r: $r=1-\frac{68}{231}b\epsilon^{-2}$. Here $b\ll1$ defines the poor conductivity of the plates. (In the thin plate limit, $b=\beta/\delta$ with δ the plate thickness.) The parameter ϵ is given by $R/R_c^{(0)}-1$, where R is the Rayleigh number and $R_c^{(0)}=720$ is its critical value at threshold for infinitely poorly conducting plates ($\beta=0$). The length scale in Eq. (2.3) is measured in units of $\frac{17}{231}\epsilon^{-1/2}$ times the depth of the fluid; time is given in units of $\frac{34}{231}\epsilon^{-1}$ vertical diffusion times. The field ψ plays the same role as before. In particular, the heat convection $(N-1)R/R_c$ with N the Nusselt number is proportional to the mean-square gradient of ψ.

[15]F. H. Busse and N. Riahi, J. Fluid Mech. **96**, 243 (1980).

[16]L. M. Pismen (unpublished).

[17]H. S. Greenside and M. C. Cross (unpublished).

[18]M. C. Cross, Phys. Rev. A **27**, 490 (1983).

[19]M. C. Cross, P. G. Daniels, P. C. Hohenberg, and E. D. Siggia, J. Fluid Mech. **127**, 155 (1983).

[20]Y. B. Pomeau and P. Manneville, J. Phys. (Paris) Lett. **40**, 609 (1979).

[21]F. H. Busse and J. A. Whitehead, J. Fluid Mech. **47**, 305 (1971).

[22]V. Croquette and A. Pocheau (unpublished).

[23]V. Steinberg, G. Ahlers, and D. S. Carrell (unpublished).